

Electrostatic gating and the interference of chiral Majoranas in thin slabs of magnetic topological insulators

Javier Osca^{1,2,*} and Llorenç Serra^{1,2,†}

¹*Institute for Cross-Disciplinary Physics and Complex Systems IFISC (CSIC-UIB), E-07122 Palma, Spain*

²*Department of Physics, University of the Balearic Islands, E-07122 Palma, Spain*

(Dated: July 21, 2025)

We study the interference of chiral Majoranas in a magnetic topological insulator thin slab having a grounded section proximity coupled to a superconductor and another section under the influence of top-bottom electrostatic gating. The gated section locally widens an energy gap and mediates the coupling between the quantum anomalous Hall states of the leads and the chiral Majorana states of the proximitized sector. Local and non-local conductances offer measurable hints of the existence of transport mediated by chiral Majorana modes. Local conductances on the two leads reveal characteristic oscillatory patterns as a function of the gating strength, with peculiar correlations depending on the distance between gated and proximitized sectors. A gate tunable Majorana diode effect on nonlocal conductances emerges when the chemical potential deviates from zero. We suggest a protocol to identify chiral Majorana physics based on a sequence of electrostatic gates that allows the tuning of chiral Majorana interference.

I. INTRODUCTION

In condensed matter systems, Majorana modes are zero-energy quasiparticle excitations that are their own antiparticles (see, e.g., Refs. [1–4]). They may appear as lower-dimensional modes in systems with particle-hole symmetry, such as topological superconductors [5–8]. In particular, two types of Majorana modes have attracted strong interest: a) Majorana bound states at the ends of nearly 1D superconducting systems, such as those based on semiconductors [9, 10], magnetic topological insulators (MTI) [11–13] or atomic and quantum dot chains [14, 15]; b) Majorana chiral modes that emerge as propagating states in the 1D edges of 2D MTI's, when the necessary symmetries and conditions are met [16]. Chiral Majoranas are propagating states analogous to quantum anomalous Hall (QAH) and quantum spin Hall (QSH) edge states but in superconducting materials [7, 17–19].

Both Majorana bound states and chiral modes are promising candidates for topological quantum computation [20] but their detection remains challenging. The same robustness that characterises these states also makes their detection arduous [21–25]. In particular, electrical measurements of Majorana bound states cannot easily be distinguished from those of bound Andreev levels, which may be induced by material disorder. An important aspect of chiral Majoranas, as opposed to Majorana bound states, is that they connect the different leads of a device via quasiparticle currents. These edge chiral currents offer a high degree of protection against backscattering. Therefore, it should be possible to identify distinctive interference correlations in charge transport or other quasiparticle properties in the presence of Majorana chiral modes. This would provide unambigu-

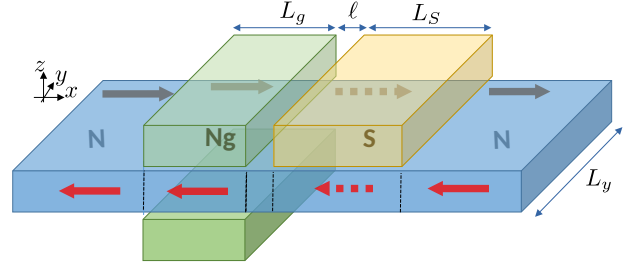


FIG. 1. Schematic of an MTI thin slab (blue) with a proximitized superconducting sector (S, superconductor in yellow) and a normal gated section (Ng, top/bottom electrodes in green). The arrows qualitatively indicate transport by chiral edge Fermionic (solid) and Majorana (dashed) modes in different sectors of the slab. The figure also shows the definitions of the transverse width (L_y) and the lengths of the proximitized (L_S), gated (L_g) and separation (ℓ) distances along the slab.

ous evidence of the existence of such topological states.

MTI's are 3D topological insulators with ferromagnetic ordering [26, 27]. It is theorized that, when in contact with a metallic s-wave superconductor, they can exhibit topological phases becoming topological superconductors in which chiral Majoranas may appear as edge states on the boundaries of MTI thin films [16, 28, 29].

In this paper, we focus on chiral Majorana physics in QAH slabs of MTI. We consider a relatively narrow QAH slab part of which is in contact with a grounded s-wave superconductor, as in Refs. [29, 30]. We also consider an additional section of the slab under the influence of a tunable perpendicular electric field (see Fig. 1). Cases of uniform gating throughout the slab have been discussed in Refs. [31–33]. The presence of a gated sector breaks

* javier.osca@uib.cat

† llorens.serra@uib.es

the left-right inversion symmetry of the device, affecting the local and nonlocal conductances in the terminals in characteristic ways depending on the topological phase of the superconductor. In this paper we refer to regions carrying the QAH state as 'normal' and regions holding chiral Majorana edge states as 'superconductor'.

By tuning the gate, correlated and anticorrelated local conductance resonances can be found in the normal leads, depending on the length L_S of the superconductor region. When a high gate potential is selected, the gate also acts as an effective electrical *cutoff*, interrupting any transmission between the two terminals. In this regime, the distance between the gate and the superconductor, denoted by ℓ , plays a significant role in the chiral Majorana phase of the superconductor. An interference of chiral Majoranas manifests as an oscillation in the conductance of the right terminal between 0 and $2e^2/h$ as a function of ℓ . This interference occurs due to the chiral Majorana injection, propagation, and reflection in the normal intermediate region. In an experiment, one could vary ℓ in a single device by activating one of a sequence of gates at a particular distance.

II. MODEL

A. Hamiltonian

We consider an MTI-based QAH thin slab containing a region of proximity-induced superconductivity. Another finite sector is under the influence of electrostatic top and bottom gates (see Fig. 1). The electrostatic gates are assumed to have reversed potentials such that a vertical electric field is induced in the slab while its mean potential remains zero. Thus, the average chemical potential in the gated sector is not shifted with respect to the other parts of the slab. It is also important to note that the gated sector breaks mirror symmetry (left-right) with respect to the proximitized sector. We will discuss below how this manifests itself on the electrical conductances.

The system Hamiltonian reads [16, 29, 30]

$$\begin{aligned} \mathcal{H} = & [m_0 + m_1 (p_x^2 + p_y^2)] \lambda_x \tau_z \\ & - \frac{\alpha}{\hbar} (p_x \sigma_y - p_y \sigma_x) \lambda_z \tau_z + \Delta_Z \sigma_z - \mu \tau_z \\ & + (\Delta_p + \Delta_m \lambda_z) \tau_x + \Delta_g \lambda_z \tau_z, \end{aligned} \quad (1)$$

where σ_{xyz} , λ_{xyz} and τ_{xyz} represent Pauli matrices for spin, layer and electron-hole spaces, respectively. The parameters m_0 and m_1 model the coupling between layers. α is the strength of the Rashba-like spin-orbit interaction, and Δ_Z is the Zeeman-like magnetization strength. The superconductivity parameters $\Delta_{p,m}$ are linear combinations of the pairing strengths in each layer. Specifically, we have that $\Delta_{p,m} \equiv (\Delta_1 \pm \Delta_2)/2$, with Δ_1 and Δ_2 the upper and lower layer pairings. Typically, these two parameters differ because the s-wave superconductor lies closer to one of the layers, with the opposite layer receiving fewer Cooper pairs. Furthermore, it is well known

that for a chiral Majorana phase these two values must differ [29].

The last term in Eq. (1) models the electrostatic-gating effect by means of the energy parameter Δ_g , which has opposite signs on the two layers due to the λ_z operator. The physical origins of the various parameters in the bilayer model have been widely discussed in literature [16, 29–36]. As mentioned, the above bilayer model has three types of two-valued pseudospins corresponding to a Nambu spinorial basis $\left[(\Psi_{k\uparrow}^t, \Psi_{k\downarrow}^t, \Psi_{-k\downarrow}^{t\dagger}, -\Psi_{-k\uparrow}^{t\dagger}), (\Psi_{k\uparrow}^b, \Psi_{k\downarrow}^b, \Psi_{-k\downarrow}^{b\dagger}, -\Psi_{-k\uparrow}^{b\dagger}) \right]^T$. We use the above Hamiltonian to describe junctions sketched in Fig. 1 by assuming that parameters $\{m_0, m_1, \alpha, \Delta_Z, \mu\}$ are constant throughout all sectors of the slab while the superconductivity $\Delta_{p,m}$ and gating Δ_g are nonvanishing only in the S and Ng regions, respectively.

Depending on the values of the magnetization, the S region of the slab may be in one of three different phases. These are the trivial phase $\mathcal{N} = 0$, a Majorana topological phase $\mathcal{N} = 1$, and a phase with two Majoranas $\mathcal{N} = 2$, where \mathcal{N} is a Majorana topological number. This corresponds to the number of chiral Majorana modes propagating along the edges of the device. We refer to the literature for detailed studies of the phase diagram with uniform parameters; particularly Refs. [29, 31, 37]. Chiral Majoranas appear in the energy band diagrams $\varepsilon(k)$ as non degenerate Dirac-like crosses inside the superconducting energy gap. The crossing point occurs at $k = 0$ and $E = 0$.

We use a numerical method to calculate the eigenfunctions within each device region, and a matching algorithm to determine the outgoing amplitudes for a given input from the asymptotic leads. Our unit system uses 1 meV as the energy unit and 1 μm as the length unit. Unless stated otherwise, in this paper we assume the following values for the Hamiltonian parameters: $\alpha = 0.2 \text{ meV}\mu\text{m}$, $m_0 = 17 \text{ meV}$, $\hbar m_1 = 10^{-3} \text{ meV}\mu\text{m}^2$, $\Delta_1 = 1 \text{ meV}$ and $\Delta_2 = 0$. The ferromagnetic magnetization parameter, Δ_Z , will be tuned to demonstrate its impact on the conductance of the various superconductor phases. This parameter physically models the intrinsic magnetization of the material. The above Hamiltonian parameters are taken as reasonable estimates for QAH insulators based on Cr doped and V doped Bi_2Se_3 magnetic thin films as discussed in Refs. [37, 38]. Nevertheless, the results discussed below are not tied to this particular set of parameters.

B. The scattering formalism

The probabilities of the device's different outgoing modes are calculated using a complex band structure analysis (see, e.g., Refs. [39, 40]). In each region of the junction, the solution is a linear superposition of left-

going, right-going and evanescent modes, given by

$$\Psi(x, y) = \sum_{k_i \sigma \tau \lambda} C_{k_i} \Phi_{\sigma \tau \lambda}^{(k_i)}(y) e^{ik_i x}, \quad (2)$$

where the k_i correspond to the set of complex wave numbers compatible with a total energy E . The C_{k_i} 's are the set of complex amplitudes in each region, and the $\Phi_{\sigma \tau \lambda}^{(k_i)}(y)$'s are the eight component spinors ($\sigma, \tau, \lambda = 1, 2$) for each complex wavenumber k_i . Right-going and left-going propagating modes are characterized by positive and negative real wavenumbers, respectively. Complex (i.e., non real) wavenumbers represent evanescent modes.

In practical terms, the set of wave numbers and eigen-spinors $\{k_i, \Phi_{\sigma \tau \lambda}^{(k_i)}\}$ is obtained by diagonalizing the k -eigenvalue problem of a homogeneous infinite slab with the same parameters as the region, for each slab sector. The values of $\{C_{k_i}\}$ are then given by a linear system representing a generalized matching algorithm at the junction interfaces. Further details of the complex band structure method can be found in Appendix A, as well as in previous Refs. 39 and 40.

Using the outgoing probability amplitudes, we can calculate the four elements of the conductance matrix,

$$\begin{pmatrix} I_L \\ I_R \end{pmatrix} = \begin{pmatrix} g_{LL} & g_{LR} \\ g_{RL} & g_{RR} \end{pmatrix} \begin{pmatrix} V_L \\ V_R \end{pmatrix}, \quad (3)$$

where $I_{L/R}$ and $V_{L/R}$ are the current and potential at the left and right leads, respectively, and $g_{ij} = \partial I_i / \partial V_j$ is the electrical conductance matrix for the different leads, $i/j = L/R$. The electric current I_i at the QAH terminals can be computed as [41]

$$I_i = \int_0^\infty dE \sum_p s_p [J_i^p(E) - K_i^p(E)], \quad (4)$$

where $p \in e, h$, with e standing for electron and h standing for hole, and $s_{e/h} = \pm 1$.

In Eq. (4) the incident current $J_i^p(E)$ is calculated as

$$J_i^p(E) = \frac{e}{h} N_i^p(E) f_i^p(E, V_i, T_i), \quad (5)$$

where $N_i^p(E)$ is the number of propagating modes of kind p in lead i , and $f_i^p \equiv 1/[1 + \exp(E - s_p e V_i)/k T_i]$ is the corresponding Fermi distribution. The lead temperatures T_i will be assumed to be negligible. Conversely, the outgoing current $K_i^p(E)$ in Eq. (4) is given by

$$K_i^p(E) = \frac{e}{h} \sum_{j,q} P_{ij}^{pq}(E) f_j^q(E, V_j, T_j), \quad (6)$$

where P_{ij}^{pq} represents the transition probability of a quasiparticle of kind q at lead j to a quasiparticle of kind p at lead i .

Note that equal indexes $i = j$ imply reflection on the same terminal while different ones $i \neq j$ imply transmission between terminals. Also note that electron and hole

quasiparticle numbers are not conserved independently at superconductor interfaces. Reflection and transmission may involve the same kind of quasiparticle or a quasiparticle swap. For example, P_{ii}^{he} is the probability of Andreev electron-hole reflection in which the number of electrons changes by two due to the formation of a Cooper pair. The resulting expressions for the conductances at vanishing temperature are

$$g_{LL} = N_L^e - P_{LL}^{ee} + P_{LL}^{he}, \quad (7)$$

$$g_{RR} = N_R^e - P_{RR}^{ee} + P_{RR}^{he}, \quad (8)$$

$$g_{RL} = P_{RL}^{he} - P_{RL}^{ee}, \quad (9)$$

$$g_{LR} = P_{LR}^{he} - P_{LR}^{ee}. \quad (10)$$

In Eqs. (7)-(10) all quantities are evaluated at an energy $E = e V_j$, with j the corresponding terminal index of the conductance matrix g_{ij} .

III. RESULTS

In this Section, we present the results of the paper on electrical properties of the system and how they are affected by the presence of the electrostatic gate. In Fig. 2 we show the band structure of the normal leads (Fig. 2a), the gated region with an electric field (Fig. 2b) and the region in contact with a superconductor (Fig. 2c). Overall, the electric field has two effects: it widens the energy gap and flattens the bands.

The widening of the gap induced by the gating in the Ng region is analogous to the effect of reducing the width L_y of the wire. Conversely, the S region, in contact with a superconductor, works as a topological superconductor. Depending on the pairings $\Delta_{1,2}$ and magnetization Δ_z , it can be in different phases labeled as $\mathcal{N} = 0$, $\mathcal{N} = 1$ and $\mathcal{N} = 2$ [31]. Figure 2c shows the typical band structure for the $\mathcal{N} = 1$ phase, in which a pair of Majorana propagating modes are present. One has $k > 0$ and the other has $k < 0$. Both have a linear dispersion relation, with each propagating in opposite edges of the device. In the $\mathcal{N} = 2$ phase two Majoranas propagate along each edge instead of one. Therefore two linear dispersion bands appear for $k > 0$ and $E > 0$ (see Appendix B and Fig. 8). In an infinitely wide system this new pair of bands is degenerate but finite-size effects break the perfect degeneracy. The trivial phase, the $\mathcal{N} = 0$ phase, has no propagating bands inside the gap in S.

The propagating modes in the normal regions N and Ng are doubly degenerate in Nambu space, for electrons and holes. Here, the charge, labelled by the quantum number $\tau_z = \pm 1$ is a proper quantum label due to the absence of any pairing $\Delta_{pm} = 0$. By contrast, the chiral Majoranas of the proximitized S region are chargeless and are equal superpositions of electrons and holes. In the limit of vanishing chemical potential, $\mu \approx 0$, the neutral character of the Majoranas is maintained over a broad range of E and k values (Fig. 2c). However, when μ starts to deviate from zero, this range shrinks to the

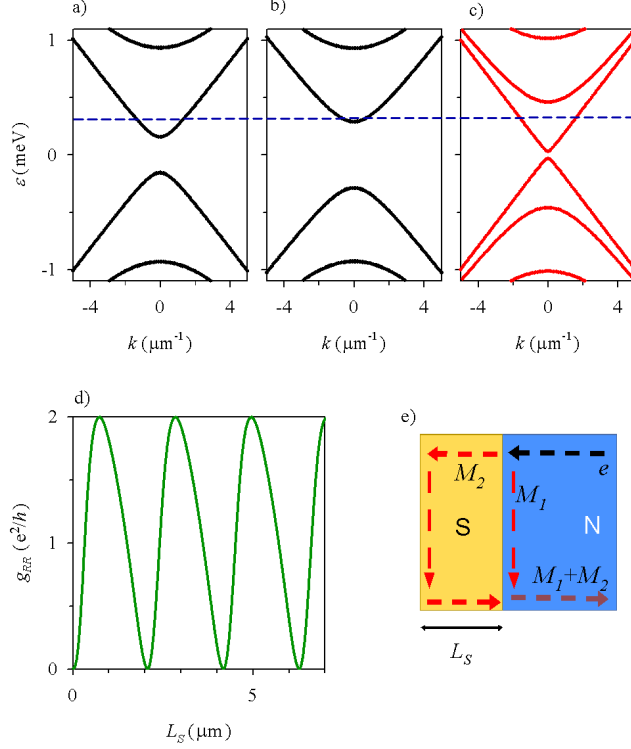


FIG. 2. a,b,c) Band structure in regions N (a), Ng (b) and S (c) of the slab sketched in Fig. 1. We used $L_y = 1 \mu\text{m}$, $\Delta_Z = 17.3 \text{ meV}$ and $\Delta_g = 3 \text{ meV}$ such that for $E = 0.3 \text{ meV}$ (dashed horizontal line) region Ng is becoming gapped. d) Local conductance in the right lead as a function of the superconductor length L_S when an intense electrostatic gating Δ_g is applied, effectively disconnecting L and R terminals. e) A schematic of the resulting interference effect when a right-incident QAH electron mode is effectively reflected into two interfering Majoranas M_1 and M_2 in lead R.

vicinity of vanishing E and k values. For this reason chiral Majorana physics is better observed in the $\mu \approx 0$ limit due to the finite size effect. In Sec. III C we discuss the initial departures from this regime that were observed in the nonlocal conductances.

A. Large Δ_g limit

It can be seen in Fig. 2b that with energy E there is a critical electrostatic gating Δ_g that, when exceeded, renders conduction in region Ng of the slab suppressed due to the absence of propagating modes. We refer to this as the cutoff regime of the gated slab. Under these conditions, the conductance g_{LL} is naturally zero at low energies. This situation is equivalent to cutting the wire electrically. However, g_{RR} still oscillates between zero and two quantum units, depending on the length of the $\mathcal{N} = 1$ superconductor region (Fig. 2d). A Fermion QAH state traveling from right to left will encounter a topo-

logical superconductor interface. As shown in Fig. 2e, half of the mode will be reflected as a Majorana M_1 on this interface, while the other half will be transmitted as a Majorana M_2 . When this last Majorana quasiparticle turns around at the virtual left edge due to the discontinuity created by the electric field, it will be reflected back to its original right lead. Both Majoranas will now run attached to the lower edge of the right lead and interfere with each other in a constructive or destructive manner, depending on their relative phase difference, which varies with the superconductor length L_S . A similar interference pattern can be obtained with a fixed superconductor length L_S but varying the energy E , which is equivalent to varying the applied right bias V_R . We stress that this remarkable interference mechanism only emerges on the right lead when the gating Δ_g is large. The variation with smaller values of the electrostatic gating is discussed next.

B. Local conductances

The local conductances g_{LL} and g_{RR} are displayed in Fig. 3, showing how they change with electric field strength for three different lengths of the superconductor. Energy and magnetization correspond to the $\mathcal{N} = 1$ phase of the superconductor. Each superconductor length represents a different scenario, with conductance peaks and valleys exactly correlated, anti-correlated or somewhere in between. These three scenarios can be distinguished by the value of g_{RR} for large Δ_g . Conversely, the g_{LL} dependence is not greatly affected by the superconductor length L_S .

When $g_{RR} \rightarrow 2e^2/h$ for large Δ_g , peaks and valleys in g_{LL} and g_{RR} are anti-correlated across the entire range of gating intensities (Fig. 3c). However, when $g_{RR} \rightarrow 0$ for high Δ_g , g_{LL} and g_{RR} are nicely correlated (Fig. 3a). Intermediate scenarios are realized for intermediate values of g_{RR} after the cutoff at large values of Δ_g . The overall behavior can be explained by realizing that as the Ng region becomes increasingly opaque g_{LL} eventually vanishes after several peaks and valleys. However, g_{RR} may eventually decrease or increase due to the Majorana interference mechanism discussed above. Therefore, Ng electrostatic gating clearly manifests the Majorana modes as a function of Δ_g . Note that the manner in which the Ng-S interface becomes opaque is not straightforward, a topic we will expand on next.

When $\Delta_g \rightarrow 0$ in Fig. 3 both g_{LL} and g_{RR} are close to e^2/h . However, the actual values may differ slightly due to the partial reflection of Majoranas caused by the finite size of the superconducting region. In the gated Ng region, the effects of finite size are greatly enhanced by increasing the value of Δ_g . Figure 4 shows the spatial distributions of the quasiparticle probability and charge for two different gating strengths, Δ_g . In the presence of an external electric field, it is possible to create low-wavenumber bulk states in the gated Ng region. These

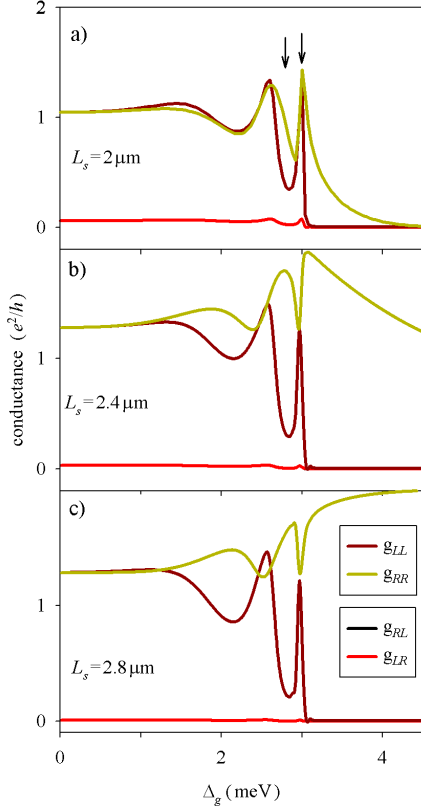


FIG. 3. Local conductances as a function of the strength of electrostatic gating Δ_g . The results in each panel correspond to a different length L_S of the superconducting region, as indicated in the figure. We assumed $L_y = 1 \mu\text{m}$, $L_g = 7 \mu\text{m}$, $\ell \approx 0$, $E = 0.3 \text{ meV}$, $\Delta_Z = 17.3 \text{ meV}$, and the other parameters are given in Sec. II A.

states result from the hybridization of a left-incident Fermionic QAH mode and a partially reflected Majorana mode at the superconductor interface. It is these low wavenumber states that are responsible for the wide oscillations in conductance seen as peaks and deep valleys in g_{LL} and g_{RR} with increasing Δ_g . The characteristic long wavelengths of these states are due to the flattening of their transport bands. The presence of these states is not exclusive of superconducting topological junctions. Similar quasibound states can also be obtained in gated sections of normal QAH slabs. However, the main difference is that, with superconductivity, the conductance peaks can rise well above the quantum of conductance.

When an integer number of half wavelengths fit within the length L_g of the gated Ng region, there is a peak in g_{LL} (see Fig. 4c,d). Conversely, if this number is a semi-integer, a conductance valley is observed (Fig. 4a,b). From the charge distributions of these states, we can see that, in Fig. 4b, an electron from the upper left is reflected also as an electron in the lower left, thus the minimum in g_{LL} . On the other hand, Fig. 4d shows a vanishing electron reflection, or even a slight Andreev pos-

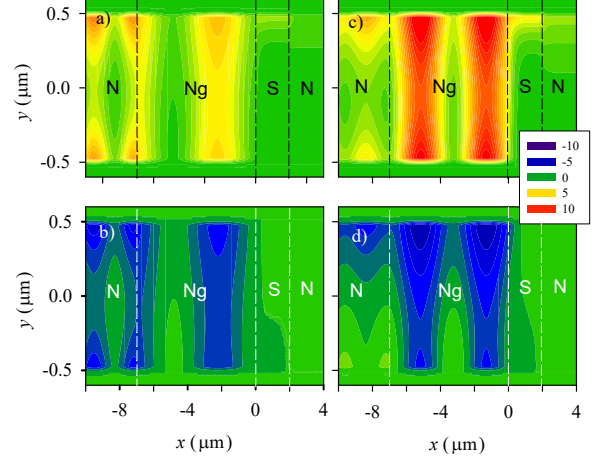


FIG. 4. Probability density distributions (a, c) and charge density distributions (b, d) in the various junction regions corresponding to a left-incidence electron mode when $L_g = 7 \mu\text{m}$ and $L_S = 2 \mu\text{m}$, as in Fig. 3a. The strength of the electric field is $\Delta_g = 2.85 \text{ meV}$ in panels a) and b), and 3 meV in panels c) and d). These two values of Δ_g correspond to the conductance dip and peak indicated with arrows in Fig. 3a.

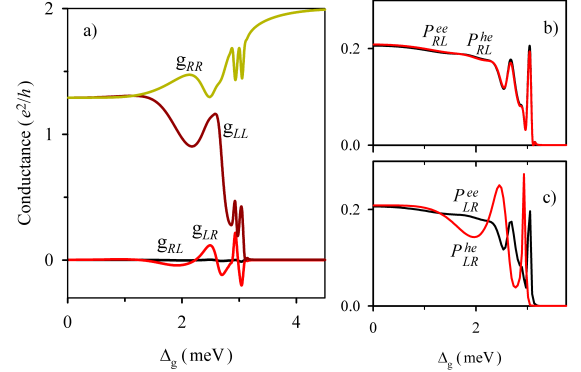


FIG. 5. a) Conductances similar to Fig. 3c but with a chemical potential $\mu = 5 \times 10^{-3} \text{ meV}$. The corresponding $L \rightarrow R$ and $R \rightarrow L$ transmission probabilities are shown in panels b and c, respectively. The $L \rightarrow R$ transmissions for electrons and holes are identical (b). Differences are clearly visible for $R \rightarrow L$ (c). This manifests as a directional asymmetry in the nonlocal conductances with a non-vanishing g_{LR} , as shown in panel a.

itive charge reflection, causing a maximum in g_{LL} conductance.

C. Non-local conductances

Non-local conductances offer an alternative view. In Fig. 3, both g_{LR} and g_{RL} are effectively vanishing over the entire range of gate intensities. This can be under-

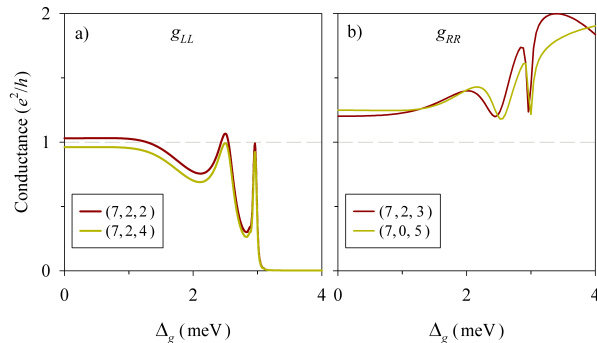


FIG. 6. Local conductances with nonvanishing Ng-S distance ℓ . The figure keys provide the distances (L_g, ℓ, L_S) in microns. The rest of parameters are the same as in Fig. 3.

stood by noting that in the limit of $\mu \approx 0$ quasiparticle transmissions between terminals are identical and independent of particle type; i.e., $P_{RL}^{ee} = P_{RL}^{he} = P_{LR}^{ee} = P_{LR}^{he}$. Deviations from this behavior when slightly increasing μ are first seen in the nonlocal conductances, as shown in Fig. 5. Even a rather small μ is enough to yield sizeable nonlocal conductance oscillations in g_{LR} (Fig. 5a), while g_{LL} , g_{RR} and g_{RL} remain in the $\mu \approx 0$ scenario. Nonvanishing g_{LR} and vanishing g_{RL} correspond to the emergence of a Majorana diode effect, which is tunable via electrostatic gating [42].

The physics in Fig. 5 can be understood from the asymmetry of the device. A right-going QAH edge state from the left terminal first traverses the electric field, followed by the topological superconductor. In contrast, a left-going edge state traverses the regions in reversed order. The probabilities of a chiral Majorana $S \rightarrow N$ injecting an electron or a hole are identical (Fig. 5b). However, these probabilities differ for a chiral Majorana $S \rightarrow Ng$ injection (Fig. 5c). This asymmetry is highly sensitive to the chemical potential μ . It vanishes in the strict $\mu = 0$ limit, but yields sizeable deviations in the non-local conductances at rather small values of μ that do not greatly affect the local conductances.

D. Role of Ng-S spacing ℓ

In this section, we consider the role of the distance between the normal gated (Ng) and proximitized superconducting (S) sectors of the MTI slab, labeled as ℓ in Fig. 1. In all previous results, we assumed that this distance was approximately zero. Here, we focus on how the presence of an intermediate normal sector (see Fig. 1) modifies the local conductances g_{LL} and g_{RR} . We find that, for $\mu \approx 0$, the non-local conductances vanish again in the presence of this distance.

The role of the distance ℓ is different for the left g_{LL} and right g_{RR} conductances. In fact, when all three distances (L_g, ℓ, L_S) are considered, the left conductance

g_{LL} is not very sensitive to L_S . As shown in Fig. 6a the overall dependence on the electrostatic gating, especially the resonant peaks before the effective cutoff for $\Delta_g \gtrsim 1$ meV, is qualitatively similar for fixed L_g and ℓ , but with different L_S values. This is reasonable in view of the quasi-confined state mechanism discussed above, which essentially depends on the left incidence conditions, which are the relevant ones for g_{LL} .

For the right terminal conductance (g_{RR}) we find that systems with a given L_g and a given value of $\ell + L_S$ show very similar results, even when L_S and ℓ differ (Fig. 6b). This effective dependence on $\ell + L_S$ can be understood in terms of the propagation of a chiral Majorana. Indeed, a left-propagating chiral Majorana injected from S into the intermediate normal region of length ℓ preserves its Majorana character also in the normal region. Therefore, in the presence of a chiral Majorana in S, g_{RR} does not distinguish between the systems with (ℓ, L_S) and $(\ell' = 0, L'_S = L_S + \ell)$. As shown in Fig. 6b, this qualitative similarity holds true for all gating intensities, including the resonance peaks and the large conductance in the wire cutoff regime.

The distance ℓ provides a way to mimic the chiral Majorana g_{RR} conductance of a longer proximitized sector L_S with a shorter one L'_S , such that $L_S = L'_S + \ell$. This can be important since the coherence length of Cooper pairs in the superconductor that gives rise to the proximity effect in the S region is usually much shorter than that of the QAH edge modes. Therefore, an intermediate slab sector of distance ℓ can be a practical way to avoid the need for very large values of L_S while still retaining the chiral Majorana quantum coherence.

E. A chiral Majorana protocol

The above results suggest a protocol for identifying the presence of a chiral Majorana mode in a proximitized MTI slab, based on a sequence of multiple side electrical gates (Fig. 7). By applying a large Δ_g to a selected gate, while keeping the others at zero gating, one can perform an effective wire cutoff at different distances from the proximitized superconducting region. Importantly, this can be achieved purely by electrical means with a single device, eliminating the need to fabricate multiple devices of different lengths of proximitized superconductor from scratch.

Specifically, we propose the following two-step protocol to identify the chiral Majorana scenario:

- With $\Delta_g = 0$ in all gates, $g_{LL} \approx g_{RR} \approx e^2/h$;
- With a large Δ_g in a selected single gate, $g_{LL} \approx 0$ while g_{RR} takes values between 0 and $2e^2/h$ depending on the distance ℓ of that particular gate to the S sector.

Condition a) is equivalent to the original chiral Majorana signature discussed in Ref. [29]. While a) is indeed a necessary condition for chiral Majoranas, it was later shown

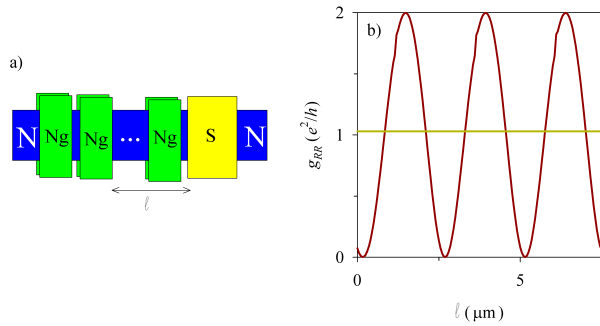


FIG. 7. a) Sketch of an MTI slab (blue) proximitized on top with a superconductor (yellow) and with a sequence of top-bottom electrostatic gates (green) to the left of the superconductor. b) Dependence of g_{RR} with the distance ℓ between the superconducting region and the electrode that electrically cuts the wire. The horizontal line shows the reference value $g_{RR} = e^2/h$ when all the electrodes are set to zero. Parameters: $E = 0.3$ meV, $\Delta_Z = 17.3$ meV, $\Delta_g = 7$ meV, $L_g = 7$ μm , $L_S = 2$ μm .

to be insufficient, as it can be mimicked in a non Majorana scenario where an incident QAH edge mode equilibrates in the superconductor emitting electron and holes with equal probabilities [21, 24, 43, 44]. This mechanism would be ruled out by requirement b). In fact, this second requirement proves the quantum mechanical interference between the two chiral Majoranas M_1 and M_2 discussed in Fig. 2 and therefore it provides a much more solid complementary evidence. Interferometric conditions in a different setup, with a circular Corbino geometry were discussed in Ref. [45].

Note that the above interferometric behavior differs from that suggested in Ref. [30], where reducing the distance L_y led to interference between the two edges. The present chiral Majorana conditions a) and b) still apply even for large L_y 's such that the two edges do not overlap significantly. The only requirement is the possibility of creating an electric cutoff by electrostatic gating at varying distances of the proximitized region. This can also be viewed as probing the nonlocality of the extended chiral Majorana state, as it is affected by an operation (electrostatic gating) performed at a distance of the superconducting region.

IV. CONCLUSIONS

Electrically gating a section of a QAH slab that also has a superconducting proximitized section offers inter-

esting ways of probing the transport properties related to chiral Majorana physics. A gap in the spectrum opens locally in the gated part. This allows tuning of the local conductances in the left and right terminals by means of the gating strength Δ_g . In the Majorana phase of the proximitized slab, resonances in the local conductances are observed. These resonances are a function of the gating strength due to the resonant coupling with localized states in the gated part of the slab. These local conductance resonances can exceed e^2/h and they are either correlated or anticorrelated depending on the length of the proximitized sector L_S , or more precisely on the total length $\ell + L_S$ where ℓ is the distance from the gated to the superconducting sectors. The resonances can also be viewed as a function of energy (applied bias). Non-local conductances usually vanish, but when the chemical potential is increased from zero, an asymmetry with nonvanishing right-to-left nonlocal conductance emerges. This mechanism has been suggested as a gate-controlled Majorana diode effect on nonlocal conductances.

For strong gating, an electrical cutoff regime is found in which the left and right terminals are effectively disconnected. In this regime, a chiral Majorana yields large oscillations between 0 and $2e^2/h$ of the right local conductance as a function of $\ell + L_S$, while all other conductances vanish. Based on this, a protocol has been suggested to identify a chiral Majorana phase. This requires a proximitized QAH slab with multiple side electric gates. In the two-Majorana (Fermionic) phase the scenario of a QAH mode propagating throughout the slab is obtained: local conductances are identical, they do not exceed e^2/h as a function of Δ_g and they tend to vanish in the electrical cutoff regime.

ACKNOWLEDGMENTS

This project is financially supported by MCIN/AEI/10.13039/501100011033 under project PCI2022-132927 of the QuantERA grant MAGMA, under project PID2023-151975NB-I00 and by the European Union NextGenerationEU/PRTR.

[1] J. Alicea, New directions in the pursuit of Majorana fermions in solid state systems, Rep. Prog. Phys. **75**, 076501 (2012).

[2] C. W. J. Beenakker, Search for Majorana fermions in superconductors, Annu. Rev. Condens. Matter Phys. **4**, 113 (2013).

- [3] S. R. Elliott and M. Franz, Colloquium: Majorana fermions in nuclear, particle, and solid-state physics, *Rev. Mod. Phys.* **87**, 137 (2015).
- [4] M. Sato and S. Fujimoto, Majorana fermions and topology in superconductors, *J. Phys. Soc. Jpn.* **85**, 072001 (2016).
- [5] A. P. Schnyder, S. Ryu, A. Furusaki, and A. W. Ludwig, Classification of topological insulators and superconductors in three spatial dimensions, *Phys. Rev. B* **78**, 195125 (2008).
- [6] A. Kitaev, Periodic table for topological insulators and superconductors, in *AIP conference proceedings*, Vol. 1134 (American Institute of Physics, 2009) pp. 22–30.
- [7] X.-L. Qi and S.-C. Zhang, Topological insulators and superconductors, *Rev. Mod. Phys.* **83**, 1057 (2011).
- [8] M. Sato and Y. Ando, Topological superconductors: a review, *Rep. Prog. Phys.* **80**, 076501 (2017).
- [9] E. Prada, P. San-Jose, M. W. A. de Moor, A. Geresdi, E. J. H. Lee, J. Klinovaja, D. Loss, J. Nygård, R. Aguado, and L. P. Kouwenhoven, From Andreev to Majorana bound states in hybrid superconductor–semiconductor nanowires, *Nat. Rev. Phys.* **2**, 575 (2020).
- [10] K. Laubscher and J. Klinovaja, Majorana bound states in semiconducting nanostructures, *J. Appl. Phys.* **130**, 081101 (2021).
- [11] Y. Zeng, C. Lei, G. Chaudhary, and A. H. MacDonald, Quantum anomalous Hall Majorana platform, *Phys. Rev. B* **97**, 081102 (2018).
- [12] C.-Z. Chen, Y.-M. Xie, J. Liu, P. A. Lee, and K. T. Law, Quasi-one-dimensional quantum anomalous Hall systems as new platforms for scalable topological quantum computation, *Phys. Rev. B* **97**, 104504 (2018).
- [13] O. Atanov, W. T. Tai, Y.-M. Xie, Y. H. Ng, M. A. Hammond, T. S. Manfred Ho, T. H. Koo, H. Li, S. L. Ho, J. Lyu, S. Chong, P. Zhang, L. Tai, J. Wang, K. T. Law, K. L. Wang, and R. Lortz, Proximity-induced quasi-one-dimensional superconducting quantum anomalous Hall state, *Cell Rep. Phys. Sci.* **5**, 101762 (2024).
- [14] S. Nadj-Perge, I. K. Drozdov, J. Li, H. Chen, S. Jeon, J. Seo, A. H. MacDonald, B. A. Bernevig, and A. Yazdani, Observation of Majorana fermions in ferromagnetic atomic chains on a superconductor, *Science* **346**, 602 (2014).
- [15] J. D. Sau and S. D. Sarma, Realizing a robust practical Majorana chain in a quantum-dot-superconductor linear array, *Nat. Commun.* **3**, 964 (2012).
- [16] X.-L. Qi, T. L. Hughes, and S.-C. Zhang, Chiral topological superconductor from the quantum Hall state, *Phys. Rev. B* **82**, 184516 (2010).
- [17] M. König, H. Buhmann, L. W. Molenkamp, T. Hughes, C.-X. Liu, X.-L. Qi, and S.-C. Zhang, The quantum spin Hall effect: Theory and experiment, *J. Phys. Soc. Jpn.* **77**, 031007 (2008).
- [18] C.-Z. Chang, J. Zhang, X. Feng, J. Shen, Z. Zhang, M. Guo, K. Li, Y. Ou, P. Wei, L.-L. Wang, Z.-Q. Ji, Y. Feng, S. Ji, X. Chen, J. Jia, X. Dai, Z. Fang, S.-C. Zhang, K. He, Y. Wang, L. Lu, X.-C. Ma, and Q.-K. Xue, Experimental observation of the quantum anomalous Hall effect in a magnetic topological insulator, *Science* **340**, 167 (2013).
- [19] G. Qiu, P. Zhang, P. Deng, S. K. Chong, L. Tai, C. Eckberg, and K. L. Wang, Mesoscopic transport of quantum anomalous Hall effect in the submicron size regime, *Phys. Rev. Lett.* **128**, 217704 (2022).
- [20] C. Nayak, S. H. Simon, A. Stern, M. Freedman, and S. Das Sarma, Non-abelian anyons and topological quantum computation, *Rev. Mod. Phys.* **80**, 1083 (2008).
- [21] M. Kayyalha, D. Xiao, R. Zhang, J. Shin, J. Jiang, F. Wang, Y.-F. Zhao, R. Xiao, L. Zhang, K. M. Fijalkowski, P. Mandal, M. Winnerlein, C. Gould, Q. Li, L. W. Molenkamp, M. H. W. Chan, N. Samarth, and C.-Z. Chang, Absence of evidence for chiral Majorana modes in quantum anomalous Hall-superconductor devices, *Science* **367**, 64 (2020).
- [22] M. Quantum, InAs-Al hybrid devices passing the topological gap protocol, *Phys. Rev. B* **107**, 245423 (2023).
- [23] A. Uday, G. Lippertz, K. Moors, H. F. Legg, R. Joris, A. Bliesener, L. M. C. Pereira, A. A. Taskin, and Y. Ando, Induced superconducting correlations in a quantum anomalous Hall insulator, *Nat. Phys.* **20**, 1589 (2024).
- [24] A. Uday, G. Lippertz, B. Bhujel, A. A. Taskin, and Y. Ando, Non-Majorana origin of the half-integer conductance quantization elucidated by multiterminal superconductor–quantum anomalous Hall insulator heterostructure, *Phys. Rev. B* **111**, 035440 (2025).
- [25] M. A. Quantum, Interferometric single-shot parity measurement in InAs–Al hybrid devices, *Nature* **638**, 651 (2025).
- [26] Y. Tokura, K. Yasuda, and A. Tsukazaki, Magnetic topological insulators, *Nat. Rev. Phys.* **1**, 126 (2019).
- [27] C.-Z. Chang, C.-X. Liu, and A. H. MacDonald, Colloquium: Quantum anomalous Hall effect, *Rev. Mod. Phys.* **95**, 011002 (2023).
- [28] L. Fu and C. L. Kane, Superconducting proximity effect and Majorana fermions at the surface of a topological insulator, *Phys. Rev. Lett.* **100**, 096407 (2008).
- [29] J. Wang, Q. Zhou, B. Lian, and S.-C. Zhang, Chiral topological superconductor and half-integer conductance plateau from quantum anomalous Hall plateau transition, *Phys. Rev. B* **92**, 064520 (2015).
- [30] J. Osca and L. Serra, Conductance oscillations and speed of chiral Majorana mode in a quantum-anomalous-Hall 2d strip, *Phys. Rev. B* **98**, 121407 (2018).
- [31] J. Wang, B. Lian, and S.-C. Zhang, Electrically tunable magnetism in magnetic topological insulators, *Phys. Rev. Lett.* **115**, 036805 (2015).
- [32] J. Wang, Electrically tunable topological superconductivity and Majorana fermions in two dimensions, *Phys. Rev. B* **94**, 214502 (2016).
- [33] S. K. Chong, P. Zhang, J. Li, Y. Zhou, J. Wang, H. Zhang, A. V. Davydov, C. Eckberg, P. Deng, L. Tai, J. Xia, R. Wu, and K. L. Wang, Electrical manipulation of topological phases in a quantum anomalous Hall insulator, *Adv. Mater.* **35**, 2207622 (2023).
- [34] J. Wang, B. Lian, H. Zhang, and S.-C. Zhang, Anomalous edge transport in the quantum anomalous Hall state, *Phys. Rev. Lett.* **111**, 086803 (2013).
- [35] J. Wang, B. Lian, and S.-C. Zhang, Universal scaling of the quantum anomalous Hall plateau transition, *Phys. Rev. B* **89**, 085106 (2014).
- [36] B. Lian, J. Wang, and S.-C. Zhang, Edge-state-induced Andreev oscillation in quantum anomalous Hall insulator-superconductor junctions, *Phys. Rev. B* **93**, 161401 (2016).
- [37] J. Legendre, E. Zsurka, D. Di Miceli, L. Serra, K. Moors, and T. L. Schmidt, Topological properties of finite-size heterostructures of magnetic topological insulators and

- superconductors, Phys. Rev. B **110**, 075426 (2024).
- [38] E. Zsurka, C. Wang, J. Legendre, D. Di Miceli, L. Serra, D. Grützmacher, T. L. Schmidt, P. Rüßmann, and K. Moors, Low-energy modeling of three-dimensional topological insulator nanostructures, Phys. Rev. Mater. **8**, 084204 (2024).
 - [39] J. Osca and L. Serra, Complex band-structure analysis and topological physics of Majorana nanowires, Eur. Phys. J. B **92**, 101 (2019).
 - [40] D. Di Miceli, E. Zsurka, J. Legendre, K. Moors, T. L. Schmidt, and L. Serra, Conductance asymmetry in proximitized magnetic topological insulator junctions with Majorana modes, Phys. Rev. B **108**, 035424 (2023).
 - [41] C. Lambert, V. Hui, and S. Robinson, Multi-probe conductance formulae for mesoscopic superconductors, J. Phys.: Condens. Matter **5**, 4187 (1993).
 - [42] M. Nadeem, M. S. Fuhrer, and X. Wang, The superconducting diode effect, Nat. Rev. Phys. **5**, 558 (2023).
 - [43] W. Ji and X.-G. Wen, $\frac{1}{2}(e^2/h)$ conductance plateau without 1d chiral Majorana fermions, Phys. Rev. Lett. **120**, 107002 (2018).
 - [44] Y. Huang, F. Setiawan, and J. D. Sau, Disorder-induced half-integer quantized conductance plateau in quantum anomalous Hall insulator-superconductor structures, Phys. Rev. B **97**, 100501 (2018).
 - [45] B. Lian, X.-Q. Sun, A. Vaezi, X.-L. Qi, and S.-C. Zhang, Topological quantum computation based on chiral Majorana fermions, Proc. Natl. Acad. Sci. **115**, 10938 (2018).
 - [46] D. Di Miceli and L. Serra, Quantum-anomalous-Hall current patterns and interference in thin slabs of chiral topological superconductors, Sci. Rep. **13**, 19955 (2023).

Appendix A: Algorithm details

We have solved the scattering problem mentioned in Sec. II B using the complex band structure formalism [39]. This approach is well suited for describing piecewise homogenous systems, such as the MTI slab with several regions of Fig. 1. The method is computationally efficient as it does not require spatial 2D (xy) grids, but rather a 1D transverse grid (y) and a set of complex k eigenmodes for each region of uniform parameters. Consequently, the computational demand is independent of the lengths L_g , ℓ and L_S of the regions forming the junction. The algorithm is a two-step process. First, the complex k 's and their corresponding eigenmodes are obtained for each region by diagonalizing an eigenvalue problem derived from the transformation of the Bogoliubov-deGennes E -eigenproblem

$$\mathcal{H}_k \Psi_k(y) = E \Psi_k(y), \quad (\text{A1})$$

where H_k is the Hamiltonian of Eq. (1) with the replacement $p_x \rightarrow \hbar k$. The transformed k -eigenproblem reads [40]

$$\begin{pmatrix} 0 & 1 \\ -\mathcal{C}^{-1}(\mathcal{A} - E) & -\mathcal{C}^{-1}\mathcal{B} \end{pmatrix} \begin{pmatrix} \Phi_k(y) \\ k \Phi_k(y) \end{pmatrix} = k \begin{pmatrix} \Phi_k(y) \\ k \Phi_k(y) \end{pmatrix}, \quad (\text{A2})$$

In Eq. (A2) we have grouped the different contributions to the Hamiltonian, Eq. (1), by defining the operators \mathcal{A} , \mathcal{B} and \mathcal{C} as follows:

$$\begin{aligned} \mathcal{A} &= (m_0 + m_1 p_y^2) \lambda_x \tau_z \\ &+ \frac{\alpha}{\hbar} p_y \sigma_x \lambda_z \tau_z + \Delta_Z \sigma_z - \mu \tau_z \\ &+ (\Delta_p + \Delta_m \lambda_z) \tau_x + \Delta_g \lambda_z \tau_z, \end{aligned} \quad (\text{A3})$$

$$\mathcal{B} = -\alpha \sigma_y \lambda_z \tau_z, \quad (\text{A4})$$

$$\mathcal{C} = m_1 \hbar^2 \lambda_x \tau_z. \quad (\text{A5})$$

Notice that Eq. (A2) is an eigenvalue problem in an enlarged space by a factor of two, due to the additional eigenvector component $k\Phi_k$. Furthermore, since the operator of Eq. (A2) is non-Hermitian it yields k eigenvalues that can have an imaginary part. Physically, these complex- k eigenmodes are relevant close to the junction interfaces.

The second step of the algorithm involves determining the set of amplitudes $\{C_k^i\}$, see Eq. (2), corresponding to the output modes in L and R leads for a given input. In practice this involves solving a linear system obtained from the continuity conditions at the junction interfaces. The wave function must be continuous at the interfaces along x . Since the Hamiltonian Eq. (2) contains a term in p_x^2 , the first x -derivative should also be continuous at the interfaces. However, the small value of parameter m_1 means that the continuity condition on the first x -derivative is only a very small correction.

The number of k -eigenmodes in each region is truncated, including the N_k modes having $|k| \leq K$, where K is the cutoff value. We typically include $N_k \approx 100$. The continuity conditions at the interfaces are projected onto the set of complex modes in order to yield a closed linear system for the set of unknowns $\{C_k\}$. The stability and convergence of the method is controlled by increasing the number N_k of complex modes and the number N_y of y grid points. The quasiparticle velocity operator v_{qp} along the slab and the associated flux I_{qp} are defined as

$$v_{qp} \equiv \frac{\partial \mathcal{H}}{\partial p_x} = -\alpha \sigma_y \lambda_z \tau_z + 2m_1 p_x \lambda_x \tau_z, \quad (\text{A6})$$

$$I_{qp} = \Re \int dy \Psi^*(x, y) v_{qp} \Psi(x, y), \quad (\text{A7})$$

where \Re takes the real part.

The corresponding charge velocity operator v_c and current I_c are defined similarly to Eq. (A6) and (A7) adding an extra τ_z operator in Eq. (A6). The quasiparticle flux I_{qp} should be conserved but this is not necessarily true for the charge flux I_c due to the possible Andreev electron-hole transformations. As a general criterion, we make sure that quasiparticle flux conservation between input and output is fulfilled by the algorithm with a precision better than 1%.

Appendix B: $\mathcal{N} = 2$ physics

The precise $\mathcal{N} = 2$ topological phase of a superconducting slab corresponds to the emergence of a doubly degenerate Majorana cross in the $\varepsilon(k)$ spectrum of states. These two degenerate Majoranas are equivalent to a pure Fermionic mode. The transport to normal leads mediated by a Fermionic mode and that mediated by a Majorana mode showing stark differences [29]. This sharp phase-transition scenario is of course modified by finite-size effects in a real slab with L_y in the micron or submicron range. Here, the emergence of a pure Fermionic mode is more gradual as the magnetization increases, transitioning from a single Majorana mode regime to a two-Majorana mode regime. An intermediate regime exists in which the two Majoranas are not exactly degenerate, resulting in conductance beating patterns [46].

Figure 8 shows the band diagrams and conductances for two values of the slab magnetization Δ_Z . Both values are close to the phase transition point between $\mathcal{N} = 1$ and $\mathcal{N} = 2$, where an additional pair of Majorana modes emerges at the device edges. Deeper in the $\mathcal{N} = 2$ phase the expected transport signature for large L_y is equivalent to that of a QAH state in a slab without superconductivity. Therefore, in the electrical cutoff regime we expect all conductances will vanish in our system. That is, the interference oscillation of g_{RR} with L_S typical of the Majorana double reflection and interference ($M_{1,2}$ of Fig. 1ed) will be washed out deep in the $\mathcal{N} = 2$ phase.

As shown in Fig. 8, slightly before the phase transition (upper panels) the Majorana bands are not degenerate,

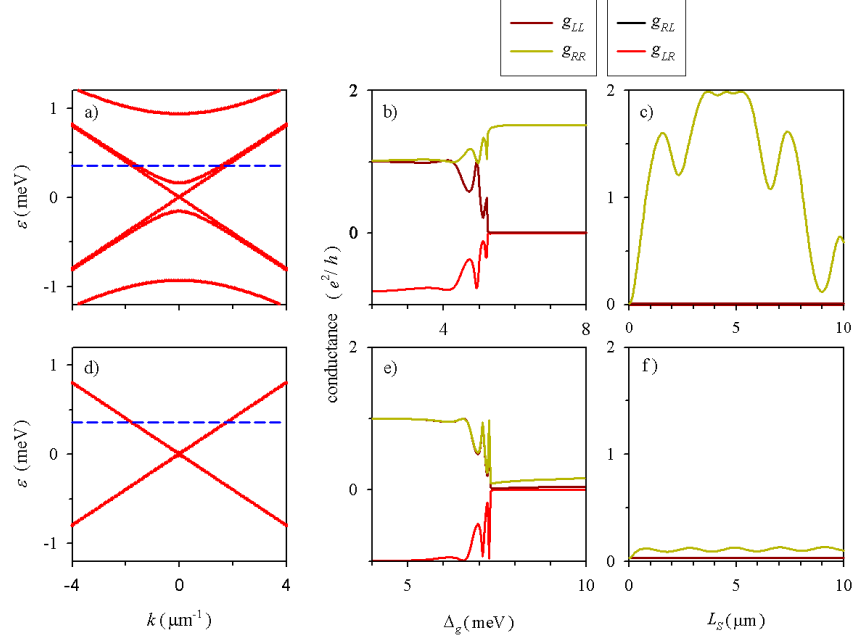


FIG. 8. a,d) Band structure in the superconducting region for a slab of $L_y = 1 \mu\text{m}$; b,c,e,f) Conductances for $L_g = 7 \mu\text{m}$, $\ell = 0$ as a function of Δ_g for a fixed $L_S = 2.8 \mu\text{m}$ (b,e), and as a function of L_S for a fixed $\Delta_g = 8 \text{ meV}$ (c,f). The upper row of panels (a,b,c) is with a magnetization $\Delta_Z = 17.8 \text{ meV}$, slightly below the $\mathcal{N} = 2$ phase transition. The lower row (d,e,f) is with $\Delta_Z = 18.5 \text{ meV}$, which is above the phase transition. The dashed blue lines in panels a) and d) indicate the assumed transport energy $E = 0.3 \text{ meV}$. Note that the Dirac cross in panel d) is doubly degenerate. The pairing strengths are $\Delta_1 = 1 \text{ meV}$ and $\Delta_2 = 0$ in all cases. Panels c) and f) are in the electrical cutoff regime due to the large Δ_g . The interference oscillation with L_S shows a multiple frequency beating pattern in panel c). This pattern indicates the activation of multiple modes, in contrast to the case of a single Majorana mode.

the local conductances g_{LL} and g_{RR} differ and display correlated oscillations. In particular, g_{RR} exhibits a pattern of multiple-frequency beating as a function of L_S in the cutoff regime (Fig. 8c). Conversely, when the magnetization is high enough, as shown in the lower panels of Fig. 8, we recover the scenario of an electronic QAH state throughout the slab, with identical g_{LL} and g_{RR} as

a function of Δ_g , not exceeding one quantum of conductance (Fig. 8e). In the cutoff regime g_{RR} becomes small, washing out the oscillations with L_S (Fig. 8f). Increasing the magnetization further, the degeneracy of the bands and the vanishing of conductances in the cutoff regime are improved.